Diffuse X-ray scattering from 180° ferroelectric stripe domains: polarization-induced strain, period disorder and wall roughness

Alexandre Boulle, Infante Ingrid C., Nathalie Lemee

Diffuse X-ray scattering from 180° ferroelectric stripe domains: polarization-induced strain, period disorder and wall roughness

A. Boulle[a], I. C. Infante[b], N. Lemée[c]

[a]Science des Procédés Céramiques et Traitements de Surface (SPCTS), CNRS UMR 7315, Centre Européen de la Céramique, 12 rue Atlantis, 87068 Limoges, France, [b]Laboratoire Structures, Propriétés et Modélisation des Solides (SPMS), CNRS UMR 8580, CentraleSupélec, Grande voie des vignes, 92295 Châtenay-Malabry, France, [c]Laboratoire de Physique de la Matière Condensée (LPMC), EA 2081, Université de Picardie Jules Verne, 33 rue Saint Leu, 80039 Amiens, France.

Abstract.

A key element in ferroic materials is the presence of walls, separating domains with different orientations of the order parameter. We demonstrate that 180° stripe domains in ferroelectric films give rise to very distinct features in their diffuse X-ray scattering (DXS) intensity distributions. A model is developed that allows to determine not only the domain period but also the period disorder, the thickness and roughness of the domain walls, and the strain induced by the rotation of the polarization. As an example, the model is applied to ferroelectric/paraelectric superlattices. Temperature-dependent DXS measurements reveal that the polarization – induced strain dramatically decreases with increasing temperature and vanishes at the Curie temperature. The motion of ferroelectric domain walls appears as a collective process that does not create any disorder in the domain period, whereas the pinning by structural defects increases the wall roughness. This work will facilitate *in-situ* quantitative studies of ferroic domains and domain wall dynamics under the application of external stimuli, including electric fields and temperature.

1. Introduction

Domains are ubiquitous among ferroic materials and are formed during phase transitions as a necessity to reduce the macroscopic manifestations of the order parameter (polarization, magnetization, strain). The ever-growing tendency for device miniaturization has led to intense research devoted to understanding ferroic materials at the nanoscale (Gregg, 2009; Catalan *et al.*, 2012). In the case of ferroelectric thin films, in order to minimize the energy of the depolarizing field and in the absence of an efficient charge screening mechanism provided, either by conducting electrodes, or surface adsorbates (Junquera & Ghosez, 2003; Fong *et al.*, 2006), the arrangement of polarization within particular spatial regions, *i.e.* domains, can be energetically favourable. Among other configurations, periodic 180° stripe domains of alternating up and down polarization (Streiffer *et al.*, 2002; Fong *et al.*, 2004; Catalan *et al.*, 2006; Takahashi *et al.*, 2008) can be spontaneously formed. The walls between adjacent domains exhibit a different structure than the bulk material, hence different properties (Seidel *et al.*, 2009), so that, at the nanoscale, where the volume concentration of walls is increasing importantly (as predicted by Kittel's law), the walls may limit or even dominate the performances of the materials (Catalan *et al.*, 2012).

In contrast with what is observed in ferromagnetic materials, it has for a long time been considered that the ferroelectric domain walls were ideally abrupt. The recent development of spherical-aberration (Cs) corrected transmission electron microscopy (TEM) has enabled the observation of ferroelectric domain walls with a finite extension over which the polarization progressively varies (Jia *et al.*, 2008), or with the local dipoles organized in vortex-like flux-closure structures, hence confining the field within the ferroelectric film (Jia *et al.*, 2011; Nelson *et al.*, 2011). Piezoresponse force microscopy (PFM) is the state of the art technique for the visualization and characterization of polar domains in ferroelectric materials (Kanilin & Bonnell, 2001; Kanilin *et al.*, 2010) and the latest developments in this technique also allowed to detect vortex structures in thin ferroelectric films (Ivry *et al.*, 2010). The occurrence of

flux-closure vortex domain structures have been predicted theoretically in ferroelectrics (Kornev *et al.*, 2004; Aguado-Puente & Junquera, 2008; Aguado-Puente & Junquera, 2012). However, unlike the magnetization in ferromagnetic materials, the electric polarization is strongly linked with the local mechanical strain and the huge ferroelastic strain associated with vortex-like structures makes them likely to occur only in very thin films, *i.e.* a few nanometers only (10 to 20 nm) (Catalan *et al.*, 2012; Jia *et al.*, 2011; Nelson *et al.*, 2011) or in nanodots (Schilling *et al.*, 2009). An additional possibility for ferroelectric materials to minimize the depolarising field, is to reorient the polarization in directions parallel to surfaces, as observed in freestanding films (Schilling *et al.*, 2006) or nanowires (Schilling *et al.*, 2007). In the case of epitaxial thin films, because of the above mention strain-polarization coupling this effect is strongly linked to the misfit strain: polarization rotation has been observed in $PbTiO_3$ ultra-thin films (Catalan *et al.*, 2006) and $PbTiO_3/CaTiO_3$ superlattices (Sinsheimer *et al.*, 2012), both under tensile strain conditions. A recent study has demonstrated that the presence of thin paraelectric ($SrTiO_3$) layers in tricolor $PbTiO_3$ / $SrTiO_3$ / $PbZr_{0.2}Ti_{0.8}O_3$ superlattices modifies the electrostatic coupling between the ferroelectric layers and and a rotation of the polarization was also observed in these systems (Lemée *et al.*, 2015). The influence of the rotation of the polarization on the state of strain in the ferroelectric materials is a question that remains to be clarified.

The analysis of the structure of domain walls and polarization – induced strain is an extremely challenging task, and even local probe techniques (such as PFM) are pushed to their limits. The above mentioned Cs-corrected TEM, albeit being probably the most powerful technique, can hardly be envisioned on a routine basis. In this work, we show that 180° stripe domains give rise to distinct features in the diffuse X-ray scattering (DXS) intensity profiles of these materials. While X-ray diffraction (XRD) is commonly used to characterize 180° stripe domains in ferroelectric films (Streiffer *et al.*, 2002; Fong *et al.*, 2004; Catalan *et al.*, 2006; Takahashi *et al.*, 2008; Highland *et al.*, 2014) and superlattices (Zubko *et al.*, 2010; Jo *et al.*, 2011; Zubko *et al.*, 2012; Chen *et al.*, 2013; Lemée *et al.*,

2015; Bein *et al.*, 2015), it is mostly restricted to the determination of the stripe period. We demonstrate hereinafter that the DXS intensity distribution can be exploited to determine the complete domain size distribution (domain randomness) and other nanostructural parameters, such as the domain wall thickness and wall roughness, and the statistical distribution of the polarization – induced strains. In particular, we derive a scattering equation that allows to model experimental DXS data and quantitatively determine all these parameters.

As an example, we apply our modeling to ferroelectric/paraelectric superlattices (SLs) which constitute ideal systems to analyze ultra-thin layers while keeping the overall material thickness large enough for being electrically and structurally investigated, also offering the possibility to engineer the strain and/or the polarization in the layer stack (Jo, Sichel, Dufresne *et al.*, 2010; Jo, Sichel, Lee *et al.*, 2010; Zubko *et al.*, 2010; Jo *et al.*, 2011; Zubko *et al.*, 2012; Sinsheimer *et al.*, 2012; Chen et al., 2013; Bein *et al.*, 2015). These ferroelectric/paraelectric SLs exhibit 180° stripe domains (Zubko *et al.*, 2010; Zubko *et al.*, 2012; Lemée *et al.*, 2015) since the paraelectric layers modify the electrical boundary conditions and induce a strong depolarizing field. In particular, in the weak electrostatic coupling regime (Stephanovich *et al.*, 2005), each ferroelectric layer in the stack behaves as an isolated entity independent from the neighbouring ferroelectric layers which therefore exacerbates effects that are usually restricted to ultra-thin films.

2. Experimental details

We have grown tricolor $PbTiO_3$ / $SrTiO_3$ / $PbZr_{0.2}Ti_{0.8}O_3$ (PT/STO/PZT) SLs on TiO_2-terminated (001)-oriented STO substrates using pulsed laser deposition following a procedure described by Hubault *et al.* (2011). The SLs are built from 20 repetitions of $PT_9/STO_2/PZT_{10}/STO_2$ units where the subscripted numbers denotes the number of unit-cells (uc) in each layer of the stack.

XRD measurements were carried out from room temperature (RT) up to 900 K in air using an in-house

designed diffractometer permitting high-resolution measurements. This diffractometer is based on a 18 kW rotating anode generator coupled with a parabolic mirror and divergence slits as primary optics, and a Ge analyzer and receiving slits as secondary optics, combined with a scintillator counter. These studies were performed using monochromatic Cu $K_{\alpha 1}$ radiation with a beam divergence estimated to 0.04° (full-width at half-maximum) with a Gaussian angular distribution. The alignment of the Ge analyzer (and the wavelength selection) is performed using a polycrystalline gold sample as a reference.

Rocking scans around symmetrical 00*l* reflections where achieved by varying incidence angle while keeping a fixed 2θ diffraction angle. The resulting profiles are solely sensitive to the in-plane structure of the films (Pietsch *et al.*, 2004). In the following, these in-plane DXS profiles are plotted as a function of the in-plane component q_x of the reduced scattering vector ($\mathbf{q} = \mathbf{Q} - \mathbf{Q}_B$), $\mathbf{Q}_B$ being the scattering vector at the center of the Bragg peak. The *x* axis is normal to the ferroelectric domain walls and the *z* axis is normal to the surface, Fig. 1(c).

DXS profiles recorded around the 001 and 002 reflections are displayed in Fig. 1(a). Two symmetric satellite reflections are clearly visible around the main Bragg peak evidencing the existence of a superstructure. Their position is independent on the reflection order which is characteristic of size-induced effects, as expected from 180° stripe domains of alternating up and down polarization. The polar origin of the observed superstructure is confirmed from the fact that the satellite reflections progressively vanish upon increasing temperature and disappear at T_C, estimated to 775 K [1], as shown in Fig. 1(b). Similar values of T_C have been observed for 10 uc-thick PT films grown on STO (Fong *et al.*, 2006; Streiffer *et al.*, 2002; Fong *et al.*, 2004) and in PT_{10}/STO_{10} SLs (Zubko *et al.*, 2012) in the weak coupling regime, suggesting that, despite the very low thickness of the STO layers in our SLs (2 uc) the ferroelectric layers are weakly electrostatically coupled (as expected in situations where the

1 The satellites reappear at their exact same location upon cooling down.

domain size in smaller than the SL period (Stephanovich *et al.*, 2005). This can be further confirmed by the stripe period Λ, estimated to 9 nm from the satellites positions at room temperature, which is close to the 7 nm period theoretically expected from 10 uc-thick PT films (Streiffer *et al.*, 2002).

3. Structural model of 180° stripe domains

The presence of in-plane satellites occurring at $2\pi / \Lambda$ can be straightforwardly explained using the simple geometry depicted in Fig. 1(c) (Streiffer *et al.*, 2002; Takahashi *et al.*, 2008; Zubko *et al.*, 2010). However, as shown in Fig. 2(a), the scattering profile from such a simple structure exhibit multiple satellite reflections and interference fringes that are usually not observed in actual DXS profiles (Fig. 1). This suggests that this geometry is an oversimplification that doesn't capture the structural complexity of ferroelectric domain structures. We here develop a structural model that allows an accurate description of DXS profiles from stripe domain structures and, hence, permits the quantification of key nanostructural features such as the complete domain period distribution, the wall thickness and roughness and polarization-induced strains. It can here be noted that we focus on spontaneously formed periodic structures in nanometric films which are significantly disordered as compared to periodically-poled lateral hetero-structures in single crystals. In the present study we can safely use the kinematical theory of diffraction. On the contrary, in high-quality periodic structures, the kinematical theory was shown to be inappropriate and a another formalism should be used (Lyford *et al.*, 2015).

3.1 Morphology of the domains

The basic building block of the model is depicted in Fig. 1(c). In a 180° stripe domain structure, the polarization varies periodically (with period Λ) from an upwards to a downwards orientation. At the

interface between two adjacent domain, there is a region (the domain wall) where the magnitude of the polarization strongly varies over very short distances. The shape of the polarization profile is commonly, though arbitrarily, described using sigmoidal functions, like a hyperbolic tangent for instance (Catalan *et al.*, 2012). In this work, for algebraic convenience and because of its strong resemblance with a tanh function, we choose to model the gradient with another sigmoidal function: the cumulative Gaussian function with standard deviation σ_w. With this description the thickness of the domain wall is $\delta = 6\sigma_w$ (*i.e.* $\pm 3\sigma_w$)[2]. The intensity scattered from such a structure can be written (the derivation is given in Appendix 1):

$$I(q_x) = \frac{\sin^2(q_x N \Lambda/2)}{2\sin^2(q_x \Lambda/2)} e^{-q_x^2 \sigma_w^2} \times \left\{ \left| F_{\uparrow} \mathrm{sinc}\left(\frac{q_x f \Lambda}{2}\right) f\Lambda + F_{\downarrow} e^{i q_x \Lambda/2} \mathrm{sinc}\left[\frac{q_x (1-f)\Lambda}{2}\right](1-f)\Lambda \right|^2 + \left| F_{\downarrow} \mathrm{sinc}\left[\frac{q_x (1-f)\Lambda}{2}\right](1-f)\Lambda + F_{\uparrow} e^{i q_x \Lambda/2} \mathrm{sinc}\left(\frac{q_x f \Lambda}{2}\right) f\Lambda \right|^2 \right\} \quad (1)$$

where $F_{\uparrow}$ and $F_{\downarrow}$ are the structure factors from up and down domains, respectively, f is the volume fraction of up domains (1/2 in the absence of an electric field) and N is the number of periods in the coherently diffracting domains. The first term on the right-hand side in Eq. 1 is due to the periodic superstructure and gives rise to additional satellite peaks occurring at $q_x = t \times 2\pi / \Lambda$ (where t is an integer). The last term, within braces, is the overall envelope of the diffraction curve and it depends on the structure factor F, the period Λ and the volume fraction f. It can be seen the domain wall affects the diffraction curve through a simple Debye-Waller – like factor, $\exp(-q_x^2\ \sigma_w^2)$, which is actually a consequence of the choice of using a cumulative Gaussian to describe the polarization gradient. Fig. 2 presents the simulated 002 DXS profiles from PT/STO/PZT SLs. A typical DXS curve computed with Eq. 1, assuming 250 nm wide coherently diffracting domains and a period Λ = 10 nm, is given in Fig.

2 This comes from the so-called three-sigma rule: 99.7% of the area of Gaussian function is contained within ± 3 standard deviations around the mean value. Since the cumulative Gaussian function is the integral of a Gaussian function, the step-width of the cumulative gaussian function (i.e. the range over which it varies from 0 to 1) can also given by the three-sigma rule.

2(a).

As noted earlier, this curve exhibits multiple interference fringes that are usually not observed in experimental data. One possible reason for this lack of fringes is a disorder in the domain period, the so-called “domain randomness” (Takahashi *et al.*, 2008). It is indeed highly unlikely that the period of the spontaneously formed domain superstructure is exactly constant over the macroscopic dimensions probed by the X-ray beam which, in turn, produces a broadening of the satellite reflections. The corresponding intensity can be simply written as the sum of scattered intensities weighted by the probability density function (pdf) of the period, p_Λ:

$$\langle I(q_x)\rangle = \int p_\Lambda(\Lambda) I(q_x, \Lambda) d\Lambda \qquad (2)$$

Fig. 2 (a-c) illustrate the effect of increasing domain randomness, which indeed yields a broadening of the satellite reflections and the smearing of the interference fringes (notice though that the width of the central peak remains unchanged). The exact shape of the pdf depends on the particular type of period disorder present in the material. Assessing the exact nature of the period disorder might be a difficult task. In our case, it was found that a lognormal distribution with standard deviation σ_Λ gives very satisfactory results. Although this choice is somewhat arbitrary, it often provides satisfactory results in systems exhibiting a certain degree of polydispersity (Boulle *et al.*, 2006) (details concerning the lognormal distribution are given in Appendix 2).

A previous study of the tricolour superlattices investigated here revealed that the domains walls are spontaneously aligned with the in plane lattice vectors, hence giving rise to discrete spots in the in-plane XRD maps (Lemée *et al.*, 2015). Similar observation were made for $PbTiO_3$ ultra-thin films (Catalan *et al.*, 2006) and $PbTiO_3/CaTiO_3$ superlattices (Sinsheimer *et al.*, 2012). In some cases however, it was found that the ferroelectric domains form isotropic ring of intensity in reciprocal space (Streiffer *et al.*, 2002), instead of discrete spots, pointing to randomly oriented ferroelectric domains. In

such cases, there is an additional contribution to the broadening of the satellites which comes from the projection of the reciprocal space intensity on the (x,z) plane, with the width of this projection being entirely determined by the collimation of the beam along the y-direction. However, such rings were not observed in this work so this contribution will not be discussed any further here.

3.2 Polarization – induced strain

Besides the formation of 180° stripe domains, an additional possibility for ferroelectric materials to confine the polarization within the film is to form flux-closure domains or to reorient the polarization in the in-plane direction[3]. Because of the strain-polarization coupling, the local rotation of the polarization will necessarily give rise to significant shear strain at the interface between domains with different orientations of the polarization (other than the strictly up/down interface). Interestingly, both situations can be described using a unique phenomenological framework.

Shear strain and rigid rotations shifts the scattering vector $\mathbf{Q}_B$ out of its theoretical position. The corresponding scattering vector is then shifted by $\Delta\mathbf{Q}_B = -\underline{\underline{e}}\ \mathbf{Q}_B^0$, where $\underline{\underline{e}}$ is the strain tensor and $\mathbf{Q}_B^0$ is the theoretical scattering vector without distortions. For a symmetrical reflection, $\mathbf{Q}_B^0 = (0,\ 0,\ Q_{B,z}^0)^T$, the reduced scattering vector can therefore be written $q_x = Q_x - e_{zx}\, Q_{B,z}^0$. The off-diagonal component e_{zx} of the strain tensor denotes the presence of shear strain or rotations of the lattice planes in the SL. If e_{zx} is randomly distributed, with a pdf p_e, instead of a tilting of the reciprocal lattice point we observe a broadening of the reflections in the Q_x direction and this is direct indication of the presence of random shear strain or random rotations (i.e. mosaicity). The total diffracted intensity finally writes:

$$\langle I(q_x)\rangle = \iint p_\Lambda(\Lambda)\, p_e(e_{xz} Q_{B,z}^0)\, I(q_x)\, d\Lambda\, de_{xz} \qquad (3)$$

3 Since the direction of the polarization is restricted by symmetry of the material, a rotation of the polarization requires a change in the symmetry. For instance, the rotation away from the strict [001] direction is accompanied by a tetragonal to monoclinic transformation (Catalan *et al.*, 2006; Sinsheimer *et al.*, 2012; Lemée et al., 2015). This is further discussed in section 4.

It can be noted that with the definition of q_x given above, the integration over e_{zx} is actually a convolution operation.

The local rotation of the polarization creates a maximum shear strain $e_{zx}^{max} = (\partial u_z / \partial x)^{max} \approx \delta z / \xi$, corresponding to the angular deviation of the (00*l*) planes from the growth direction, where δz is the dimensional change of the unit-cell along the [001] direction, ξ is the distance over which the polarization rotates and u_z is the lattice displacement[4]. Because of the polydispersity of the ferroelectric domains, the distance ξ is itself a random variable, which gives rise to a random distribution of e_{zx} (with pdf, p_e) hence the observed broadening of the peaks. In the distribution of e_{zx} , most unit-cells are free of shear strain (average $\langle e_{zx} \rangle = 0$), whereas those close to the domain boundaries experience significant shear strains. Such large deviations of e_{zx} from the average value give long tails in p_e that can be accounted for using Lévy-stable distributions, which arise in the framework of the *generalized* central limit theorem[5]. Hereinafter, pseudo-Voigt functions are used to model Levy-stable distributions since these distributions lack closed-form analytical formula (details regarding Levy-stable functions are given in Appendix 2). Within this model, the tail index η takes values between 0 (for a Gaussian distribution with $\exp(-q_x^2)$ asymptotic behavior) and 1 (for a Lorentzian distribution exhibiting $1/q_x^2$ tails). Intermediate values of η correspond to intermediate tail behaviors which, hence, correspond to different probabilities of observing high deviations from the average value for a given width of p_e.

3.3 Simulations

In the present section we demonstrate how the different effects described above can be disentangled by a careful examination of the DXS curve. The limits of the modelling are also discussed.

---

4 In this work we don't use the average (symmetrized) shear strain $e_{zx} = (\partial u_z/\partial x + \partial u_x/\partial z)/2$, because this definition cancels rigid rotations which are indeed measured in the diffraction experiment.

5 The generalized central limit theorem is a reformulation of the central limit theorem with the condition of finite variance being dropped. See W. Feller *et al.* (1970).

Simulated DXS curves of the 002 reflections, corresponding to 250 nm – wide coherent domains with Λ = 10 and increasing domain randomness (σ_Λ = 0, 1, 3 nm), shear strain (ε_{zx} = 0, 0.1, 0.3°) and wall thickness (σ_w = 0, Λ/12) are depicted in Fig. 2. Fig. 2 (a,b,c) illustrates the effect of increasing domain randomness, which, as already noted in Sec. 3.1, yields the broadening of the satellite reflections and the smearing of the interference fringes while the width of the central peak remains unchanged. Fig. 2(a,d,g) illustrate the effect of shear strain. In each panel, the three curves correspond to three values of the tail index (η = 0, 0.5 and 1). Contrarily to what is observed with domain randomness, random shear strain broadens the whole DXS curve (*i.e.* the satellites and the central peak). Both type of defects can therefore be clearly distinguished. Increasing the tail index of the shear strain distribution significantly modifies the shape of the central and satellite peaks and results in DXS profiles with more pronounced profile tails.

The other panels in Fig 2 (e, f, h, i) show simulations with both the effects of shear strain and domain randomness. This figure shows that these parameters distinctly affect the DXS which opens the way to their determination using experimental DXS data. The red dotted curve in Fig. 2 represents the action of the thickness of the domain wall. As expected from Eq. 1, the wall thickness affects the asymptotic behaviour of the curve. As compared to strain and domain randomness, its influence is relatively limited though. In these simulations we used the maximum possible value of the domain wall thickness, $\delta = \Lambda/2$ (so that $\sigma_w = \Lambda/12$) which correspond to domain walls expending throughout the whole domain with the formation of sinusoidal polarization profiles which are predicted to occur in very thin films (Luk'yanchuk *et al.*, 2009).

Fig. 3 displays simulations for several 00*l* reflections with *l* increasing from 1 to 4 and various coherent domain sizes (the other parameters being σ_Λ = 1 nm, ε_{zx} = 0.1° and η = 0.5). It is readily observed that for small coherent domains (~ 50 nm) the width and shape of the DXS curve is largely dominated by

finite size effects, with clearly visible interference fringes and broad curves, even at low values of *l*. On the contrary, for large coherent domains, (250 nm and above) it can be observed that size-induced effects are negligible: the DXS curves are extremely narrow at low *l* values, and the width of the curves scale with *l*. With the parameters used here, the curves computed with 250 nm and 500 nm – wide coherent domains are almost identical.

The divergence of the incident beam also contributes to the overall broadening of the DXS curve, through a convolution operation with the resolution function of the diffractometer. This convolution is straightforwardly performed with Eq. 3, by adding the (Gaussian) resolution function to the Gaussian part of the pseudo-Voigt function used to describe the strain pdf.

Finally it should be noted that structural defects having a similar influence on the DXS curve (but with a distinct physical nature) curve cannot be distinguished using solely XRD data, or at least one single data set. For instance, mosaicity (random rotations of lattice planes) produces exactly the same broadening of the DXS curve than polarization – induced strain. Disentangling these effects requires additional information using complementary techniques or, as shown in the next section, by making use of their distinct behaviour under the application of external stimuli, like temperature for instance.

4. Example: $PbTiO_3$ / $SrTiO_3$ / $PbZr_{0.2}Ti_{0.8}O_3$ superlattice

Eq. 3 has been used to fit DXS data from tricolor PT/STO/PZT SLs using a generalized simulated annealing algorithm (Boulle & Debelle, 2010). This global search algorithm allows to find the best possible solution for a given set of parameters and data, avoiding the shortcomings of conventional least-squares techniques associated with the presence of local minima. The results are shown in Fig. 1(a,b) as the red line. Fig. 1(a) is the simulation, with one single set of structural parameters, of both the 001 and 002 peaks recorded at room temperature. From this simulations the lateral coherent domain size was estimated to ~ 900 nm. This value was assumed to be constant with temperature and has been

used for all the temperature-dependent measurements.

In Fig. 4(a), we present the evolution with temperature of the relative out-of-plane component of the polarization deduced from the structure factor, including a fit with a $k(1 - T/T_C)^{1/2}$ law (red line) indicating that the SL behaves as a proper ferroelectric with a Curie temperature of T_C = 775 K, in agreement with the observations above. Fig. 4(b) shows the evolution of the average stripe period $<\Lambda>$ which decreases with increasing temperature. A similar trend has previously been observed in ferroelectric-paraelectric PT/STO SLs (Zubko *et al.*, 2012b). In Fig. 4(c), the evolution of the relative domain randomness ($\sigma_\Lambda / <\Lambda>$) is plotted *vs.* temperature. Also plotted is the calculated evolution with constant domain randomness (σ_Λ = 1.5 nm, blue line). From this figure it can be concluded that the observed evolution of the relative randomness is solely due to the shortening of the stripe period upon heating. In the particular case of our tricolour SLs it is unclear whether the observed randomness is due to in-plane fluctuations of the period, or to fluctuations along the growth direction or even from variations from the PT to the PZT layers. Nonetheless, since our computation assumes that both PT and PZT contributes to polarization profiles, the quality of the fit indicates that domains are present in both layers with a similar period. Moreover, the fact that no disorder in the period is created upon heating demonstrates that the displacement of the wall is collective process.

Also plotted in Fig. 4(c) is the relative effective wall thickness (σ_w / w, where $w = <\Lambda>/2$ is the domain size). The horizontal dotted line corresponds to the maximum possible relative wall thickness as given by $\sigma_w = \Lambda / 12$. Surprisingly, at room temperature, the observed relative roughness is higher than this value and it even increases for increasing temperature. This behaviour can be rationalized as follows: the DXS intensity distribution in the direction normal to the wall is actually sensitive to the projected

polarization profile along the *x* axis. Therefore if the walls are not perfectly flat on the atomic level (Fig. 4e), the projected polarization profile may also exhibit smooth variations from an up to a down domain (Fig. 4f), in a similar fashion than thick domain walls (Fig. 4d), even if the actual thickness of the domain walls is equal to zero. Using the cumulative Gaussian function introduced in Sec. III, the standard deviation, noted σ_R, then corresponds to the root-mean-squared (rms) roughness of the walls, $<\Delta u_x(\infty)^2>^{1/2}$, where u_x is the local deviation from a perfectly flat wall (Paruch *et al.*, 2005) and the infinity symbol indicate that, in the direction normal to the walls, the DXS is not sensitive to short-range correlation in the displacement difference $\Delta u_x(r)$. The wall thickness measured is actually the convolution of both contributions, *i.e.* wall thickness and wall roughness, which leads to $\sigma_w^{tot} = (\sigma_w^2 + \sigma_R^2)^{1/2}$.

In 10 nm – thick PZT films, at room temperature, Cs-corrected TEM observations (Jia *et al.*, 2008) revealed that, in the case of uncharged domain walls[6], the wall thickness equals at most two unit-cells, *i.e.* 0.8 nm, which yields to σ_w = 0.13 nm (which is an order of magnitude smaller than the values observed here). In our SLs each ferroelectric layer are at most 10 uc – thick. For ultra-thin films, theoretical work suggests that the wall thickness increases and that the polarization profile then exhibits a sinusoidal shape. Therefore, assuming the domain walls in our SLs exhibit the maximum possible thickness ($\delta = \Lambda/2$ or $\sigma_w = \Lambda / 12$) we deduce the evolution of the relative roughness (red dotted line). Although the absolute values of the roughness are uncertain (as they depend on the assumed value of the wall thickness) a neat relative increase is observed. This evolution is actually a manifestation of the dynamics of the domain walls, where the increase of the roughness is due to the pinning by structural defects during wall motion (Paruch *et al.*, 2005; Paruch *et al.*, 2012).

6 We here measure the 002 reflection which is solely sensitive to the out-of-plane component P_z of the polarization, and the corresponding measurement hence corresponds to an uncharged wall.

We finally focus on the evolution of the shear strain disorder, which can be quantified by the width of the shear strain distribution p_e, and noted ε_{zx} in Fig. 5(a). Upon increasing sample temperature, ε_{zx} decreases from 0.11° at RT to 0.05° at T_C, and then remain constant. This behaviour indicates that part of the shear strain is of polar origin and the constant part surviving above T_C is the intrinsic mosaicity of the SLs, which, as outline in Sec. 3.3, also affects the e_{zx} component of the strain tensor. These results are fully reversible after heating and cooling cycles through T_C. First, we note that above T_C the strain pdf is Gaussian ($\eta = 0$) and, as shown in Fig. 5(b) the deviations are closely confined around the central value ($e_{zx} = 0$). Using the cumulative distribution function (cdf) shown in Fig. 5(c), we also notice that, at T_C, the maximum shear strain experienced by the system is only ~0.09°. Conversely, at room temperature, the strain pdf exhibits pronounced tails ($\eta = 0.42$), Fig. 5(b), and the cdf reveals that 10% of the unit-cells experience a strain higher than 0.14° with a maximum shear strain value of ~2°.

This observation could be explained by the ferroelastic strain developing at flux-closure domains. The presence of such domains locally rotates the polarization by 90°, which exchanges the positions of the *a* and *c* direction of the unit-cell which in turn generates huge strains at the interface between *a* and *c* oriented domains, Fig. 5(d). Within this picture, the maximum shear strain e_{zx}^{max} (calculated assuming that the width of the closure stripes extend over half of an average domain on both sides of the wall, *i.e.* $\xi = w = <\Lambda>/2$) equals 0.25° and 0.33° for PZT and PT, respectively, values which are clearly included in the strain pdf observed at room temperature, and are 3 times higher than the maximum shear strain observed at T_C. It should be here recalled that the computed values of e_{zx}^{max} depend on the value of ξ, so that fluctuations in the values of ξ also give rise to fluctuation of e_{zx}^{max}, as observed in the strain distribution.

In addition, the rotation of the polarization vector can also contribute to the observed behaviour of the strain. A recent study of tricolour PT/STO/PZT SLs demonstrated (i) the presence of an in-plane

component of the polarization, as revealed by satellite reflections in in-plane XRD maps (pointing to head-to-head and tail-to-tail configurations of this component), (ii) the transition from the tetragonal phase to a monoclinic M_C phase induced by the rotation of the polarization (Lemée *et al.*, 2015). The transition to the monoclinic phase in turn gives rise to twin domains which could be detected in the XRD maps and an average monoclinic angle $\beta = 89.8$ could be determined. Fig. 5(e) schematically represents two twin domains tilted by an angle $2\Delta\beta = 0.4°$, where $\Delta\beta$ is the deviation from the tetragonal symmetry. Within each twin domain the configuration of the polarization accounts for the observed DXS satellites in the present article and in the in-plane XRD maps (Lemée *et al.*, 2015), and the tilt angle accounts for the broadening of the DXS curve in a similar fashion to mosaicity. In Ref. (Lemée *et al.*, 2015) the XRD spots emanating from the twin domains were significantly broadened and overlapped indicating a distribution in the $\Delta\beta$ angles, as observed here (on the contrary a unique $\Delta\beta$ angle would give rise to distinct peaks, and no broadening). Interestingly, the tilt angle between the twin domains (0.4°) is included in the range of strain spanned by the pdf recorded at room temperature. Both of the previous interpretations are plausible in regards of the DXS data, it is hence not possible to disentangle the action of flux-closure strain and domain twinning using solely DXS. Although domain twinning, induced by the rotation of the polarization, has been confirmed by complementary XRD measurements, flux-closure strains can not be firmly ruled out without additional characterizations.

5. Conclusions

We have shown that, when studying stripe domains, DXS offers a unique way to discriminate between morphological effects (such as the presence of domains, domain randomness and wall roughness) and strain effects that develop around regions where the polarization has different in-plane components. Combined with temperature-dependent measurements, the polar contribution to shear strain can be

clearly distinguished from the other, non-polar, contributions (*e.g.* the intrinsic mosaicity of the SLs). This work will facilitate the quantitative study of polarization – induced strains and domain wall dynamics under the application of external stimuli, including electric fields; an area of research which is witnessing an intense interest these last years for the study of ferroelectric materials (Streiffer *et al.*, 2002; Fong *et al.*, 2004; Grigoriev *et al.*, 2006; Jo, Sichel, Dufresne *et al.*, 2010; Jo, Sichel, Lee *et al.*, 2010; Zubko *et al.*, 2010; Jo *et al.*, 2011; Chen *et al.*, 2013; Bein *et al.*, 2015). In the case of the temperature-induced evolution we have demonstrated that the polarization – induced strain gradually decreases for increasing temperature and that the pinning by lattice defects results in an increased wall roughness. Besides, the displacement of the domain walls, required to reduce the stripe period, appears as a collective process as no period disorder is induced during motion.

With the advent of two-dimensional detectors now commonly available at synchrotron beamlines, the amount of information accessible by XRD techniques can be considerably increased, without increasing the measurement time (which is of particular interest for *in-situ* experiments). In the case of ferroelectric domains occurring in SLs, the acquisition of full three-dimensional (3D) reciprocal space maps allows one to probe both the evolution of the in-plane domain structure and the out-of-plane structure of the SLs. For instance in the case domains developing along the main [100] and [010] direction the in-plane profile is simply the product of two profiles (as given by Eq. 1) function of $q_{[100]}$ and $q_{[010]}$, whereas the out-of-plane intensity profile would be given by standard scattering equations applying to SLs (Pietsch *et al.*, 2004). More complex situation, for instance with non-orthogonal domains or a variation of the domain period across the thickness of the SLs might also be detected by 3D reciprocal space mapping, although the simulation of the data would require a 3D integration as compared to the simple 1D integration performed in this work (see appendix 1).

Finally it must be recalled that XRD can not be used to identify structural defects, *i.e.* different defects may may yield similar XRD curves. As with any model-dependent approach, the exact nature of the

defects has to be determined beforehand using complementary experiments.

Appendix 1

Scattering from a perfect and strain-free stripe domain structure

The domain structure consists of regions with alternating up and down polarization, with period Λ and the relative volume fraction of up/down domains is given by f (which is equal to 1/2 is the absence of an electric field), as schematically represented in Fig. 1(c). The spatial evolution of the polarization is described by the function denoted $\psi(x,a)$ which permits the polarization to vary smoothly from an up to a down domain and vice versa. A possible expression for such a function is

$$\Psi(x,a)=\Phi(x/\sigma_w)-\Phi\left[(x-a)/\sigma_w\right] \tag{A1}$$

where Φ is the cumulative Gaussian distribution function:

$$\Phi(x)=\frac{1}{2}\left[1+erf\left(\frac{x}{\sqrt{2}}\right)\right] \ , \tag{A2}$$

and σ_w is the standard deviation, so that $\delta = \pm 3\sigma_w$ corresponds to the wall thickness. It can be noticed that when σ_w tends to 0, the shape function converges to the top-hat function, $\Pi(x,a) = 1$ for $0 \le x \le a$ (0 otherwise), which correspond to a sharp domain wall. With this geometry the variation of the structure factor (consecutive to the evolution of the orientation of the polarization) in the direction normal to the domain walls can be written:

$$F_{\uparrow\downarrow}(x)=\left[\langle F_{\uparrow}\rangle\Psi(x,f\Lambda)+\langle F_{\downarrow}\rangle\Psi\left[x-f\Lambda,(1-f)\Lambda\right]\right]*\sum_{n=0}^{N-1}\delta(x-n\Lambda) \tag{A3}$$

where N is the number of periods within a coherently illuminated region (in the present case, it turned out that $N \approx 50$ provided a good agreement with the experimental data). $F_{\uparrow}$ and $F_{\downarrow}$ are the structure factors corresponding to an upwards and a downwards polarization respectively. For instance if $F_{\uparrow}$ correspond to a reflection with structure factor F_{hkl}, $F_{\downarrow}$ is then given by $F_{\overline{hkl}}$.

Since the q_x-scans are performed through central peak of the SL reflection (*i.e.* the 0th order peak), the

corresponding intensity profile is not sensitive to the SL structure, but only to the average structure factor <*F*> of the SL, where the average is performed over the multiple layers of the SL. For an upward polarization we hence obtain

$$\langle F_{\uparrow} \rangle = x_{PZT} F_{\uparrow}^{PZT} + x_{PT} F_{\uparrow}^{PT} + x_{STO} F^{STO} \tag{A4}$$

where $x_{PZT,\ PT,\ STO}$ are the volume fractions of PZT, PT and STO, respectively ($x_i = n_i / \Sigma n_i$, where n_i is the number of unit cells of each compound in a single SL period). Owing to the weak coupling regime observed in our SLs, we shall assume that STO exhibits its usual paraelectric structure. For the calculation of the structure factor of PZT and STO, we further assume that the shifts of the Zr^{4+} and Ti^{4+} ions are identical and that the displacements of the two different type of O^{2-} ions are the same (Jia *et al.*, 2007). Since the polarization, *P*, is directly proportional to the shift of the cations with respect to the O^{2-} ions, the fractional displacements are written $\delta z_{Ti} = \delta z_{Zr} = \delta z_{Ti}^{0} \times (P/P_{300})$ and $\delta z_{O} = \delta z_{O}^{0} \times (P/P_{300})$ (the origin of the unit cell being taken on the Pb^{2+} ions), where $\delta z_{Ti}^{0} = 0.039$ and $\delta z_{O}^{0} = 0.114$ are the fractional displacements of the Ti^{4+} and O^{2-} ions at room temperature, respectively (Glazer & Mabud, 1978), and P_{300} is the value of the polarization at 300 K.

In the vicinity of the reflection considered the scattered amplitude along q_x can be written can be written (Pietsch *et al.*, 2004):

$$E_{\uparrow\downarrow}(q_x) = \int F_{\uparrow\downarrow}(x) \exp(i q_x x)\, dx \tag{A5}$$

Using the expression of $F_{\uparrow\downarrow}$ (Eq. A3) we obtain:

$$E_{\uparrow\downarrow}(q_x) = E_{\Lambda}(q_x) \frac{\sin(q_x N \Lambda/2)}{\sin(q_x \Lambda/2)} e^{i q_x (N-1)\Lambda/2} \tag{A6}$$

where

$$E_{\Lambda}(q_x) = e^{-q_x^2 \sigma_w^2/2} \left\{ F_{\uparrow} \mathrm{sinc}\left(\frac{q_x f \Lambda}{2} \right) f \Lambda + F_{\downarrow} e^{i q_x \Lambda/2} \mathrm{sinc}\left[\frac{q_x (1-f) \Lambda}{2} \right] (1-f) \Lambda \right\} e^{i q_x f \Lambda/2} \tag{A7}$$

The first term on the right-hand side in Eq. (A6) determines the overall envelope of the diffraction curve and it solely depends on the period Λ, the thickness of the domain walls σ_w and the up/down volume ratio f. The second term is due to the periodic structure and gives rise to additional satellite peaks occurring at $q_x = t \times 2\pi / \Lambda$ (where t is an integer). It can be noticed that when $f = 1 / m$, then the envelope function exhibits minima at $q_x = m\ 2\pi / \Lambda$, which yields the suppression of the mth order satellites. Hence, for $f = 1/2$ only the odd orders are visible. In a standard XRD experiment the irradiated volume is in general much larger than the coherence volume of the incident beam, so that the recorded intensity is given by the incoherent superposition of the intensities emanating from different coherently irradiated regions. In these regions, the occurrence of up/down and down/up domains being, a priori, equally probable, the observed intensity is given by the average $I(q_x) = (|E_{\uparrow\downarrow}|^2 + |E_{\downarrow\uparrow}|^2) / 2$, which finally gives rise to the Eq. 1.

Appendix 2

Lognormal, Lévy-stable and pseudo-Voigt distributions

A log-normal distribution is used to model the pdf of the stripe period:

$$p_{\mathrm{LN}}(x) = \frac{1}{\sqrt{2\pi}\, x\, \sigma_{\mathrm{LN}}} \exp\left[-\frac{1}{2} \left(\frac{\ln x - \mu_{\mathrm{LN}}}{\sigma_{\mathrm{LN}}} \right)^2 \right] \tag{A8}$$

where the parameters μ_{LN} and σ_{LN} are related to the arithmetic mean μ and standard deviation σ by:

$$\mu = \exp\left(\mu_{\mathrm{LN}} + \sigma_{\mathrm{LN}}^2 / 2 \right) \tag{A9}$$

and

$$\sigma^2 = \exp\left(2\mu_{\mathrm{LN}} + \sigma_{\mathrm{LN}}^2 \right) \left[\exp\left(\sigma_{\mathrm{LN}}^2 - 1 \right) \right] \tag{A10}$$

The average period and domain randomness are computed using the the above expressions of μ and σ.

The shear strain pdf were assumed to obey a Lévy-stable distribution. There is no-closed form formula for most Lévy-stable distribution and they are in general specified by their characteristic function. In the case of a symmetrical distribution, $L_\gamma(x)$, this reads (Boulle *et al.*, 2006):

$$\int dx \cdot L_\gamma(x) \exp(iqx) = \exp\left(i\mu^0 q - \sigma^\gamma |q|^\gamma / 2\right) \quad \text{(A11)}$$

where μ^0, σ and γ are the mean of the distribution, its width and its shape, respectively. For instance, when $\gamma = 2$ we obtain a Gaussian distribution and σ is the standard deviation. When $\gamma = 1$, we obtain a Lorentzian distribution, with heavy $1/x^2$ tails, and σ is the full-width at half maximum. Since the lattice planes of the SL are, on average, parallel to the lattice planes of the substrate, the mean is $\mu^0 = 0$. In order not to impair the computation times we choose not to numerically evaluate the above Fourier transform (Eq. 6), and, instead approximate $L_\gamma(x)$ with a pseudo-Voigt function, *i.e.* the linear combination of a Gaussian function, $G(x)$, and a Lorentzian function, $L(x)$:

$$pV(x) = (1 - \eta)G(x) + \eta L(x) \quad \text{(A12)}$$

where η is the tail index. For $\eta = 0$ ($\gamma = 2$) the distribution is Gaussian and for $\eta = 1$ ($\gamma = 1$) the distribution is Lorentzian. Intermediate values of η (and $\gamma \in [1,2]$) give rise to distribution with profile asymptotically behaving between $\exp(-x^2)$ and $1/x^2$. Note that for $\eta > 1$ ($\gamma < 1$) super-Lorenzian profiles are obtain with tails behaving as $1/x^{1+\gamma}$ (Boulle *et al.*, 2006).

References

Aguado-Puente, P., Junquera, J. (2008). *Phys. Rev. Lett.* **100**, 177601.

Aguado-Puente, P., Junquera, J. (2012). *Phys. Rev. B* **85**, 184105.

Bein, B., Hsing, H.-C., Callori, S. J., Sinsheimer, J., Chinta, P. V., Headrick, R. L., Dawber, M. (2015). *Nature Comm.* **6**, 10136.

Boulle, A., Conchon, F., Guinebretière, R. (2006). *Acta Cryst. A* **62**, 11-20.

Boulle, A., Debelle, A. (2010). *J. Appl. Cryst.* **43**, 1046-1052.

Catalan, G., Janssens, A., Rispens, G., Csiszar, S., Seeck, O., Rijnders, G., Blank, D. H. A., Noheda, B. (2006). *Phys. Rev. Lett.* **96**, 127602.

Catalan, G., Seidel, J., Ramesh, R., Scott, J. F. (2012). *Rev. Mod. Phys.* **84**, 119-156.

Chen, P., Cosgriff, M. P., Zhang, Q., Callori, S. J., Adams, B. W., Dufresne, E. M., Dawber, M., Evans, P. G. (2013). *Phys. Rev. Lett.* **110**, 047601.

Feller, W. (1970). *An Introduction to Probability Theory and its Applications*, New - York: Wiley.

Fong, D. D., Stephenson, G. B., Streiffer, S. K., Eastman, J. A., Auciello, O., Fuoss, P. H., Thompson, C. (2004). *Science* **304**, 1650-1653.

Fong, D. D., Kolpak, A. M., Eastman, J. A., Streiffer, S. K., Fuoss, P. H., Stephenson, G. B., Thompson, C., Kim, D. M., Choi, K. J., Eom, C. B., Grinberg, I., Rappe, A. M. (2006). *Phys. Rev. Lett.* **96**, 127601.

Glazer, M., Mabud, S. A. (1978). *Acta Cryst. B* **34**, 1065-1070.

Gregg, J. M. (2009). *Phys. Stat. Sol. A* **206**, 577-587.

Grigoriev, A., Do, D. H., Kim, D. M., Eom, C. B., Adams, B., Dufresne, E. M., Evans, P. G. (2006). *Phys. Rev. Lett.* **96**, 187601.

Highland, M. J., Fong, D. D., Stephenson, G. B., Fister, T. T., Fuoss, P. H., Streiffer, S. K., Thompson, C., Richard, M. I., Eastman, J. A. (2014). *Appl. Phys. Lett.* **104**, 132901.

Hubault, C., Davoisne, C., Dupont, L., Perrin, A., Boulle, A., Holc, J., Kosec, M., Karkut, M.G., Lemée, N. (2011). *Appl. Phys. Lett.* **99**, 052905.

Ivry, Y., Chu, D. P., Scott, J. F., Durkan, C. (2010). *Phys. Rev. Lett.* **104**, 207602.

Jia, C. L., Nagarajan, V., He, J. Q.,Houben, L. , Zhao, T., Ramesh, R., Urban, K., Waser, R., (2007). *Nature Mater.* **6**, 64-69.

Jia, C. L., Mi, S. B., Urban, K., Vrejoiu, I., Alexe, M., Hesse, D. (2008). *Nature Mater.* **7**, 57-61.

Jia, C. L., Urban, K. W., Alexe, M., Hesse, D., Vrejoiu, I. (2011). *Science* **331**, 1420-1423.

Jo, J. Y., Sichel, R. J., Lee, H. N., Nakhmanson, S. M., Dufresne, E. M., Evans, P. G. (2010). *Phys. Rev. Lett.* **104**, 207601.

Jo, J. Y., Sichel, R. J., Dufresne, E. M., Lee, H. N., Nakhmanson, S. M., Evans, P. G. (2010). *Phys. Rev. B* **82**, 174116.

Jo, J. Y., Chen, P., Sichel, R. J., Callori, S. J., Sinsheimer, J., Dufresne, E. M., Dawber, M., Evans, P. G. (2011). *Phys. Rev. Lett.* **107**, 055501.

Junquera, J., Ghosez, P. (2003). *Nature* **422**, 506-509.

Kanilin, S. V., Bonnell, D. A. (2001). *Phys. Rev. B* **63**, 125411.

Kanilin, S. V., Morozovska, A. N., Chen, L. Q., Rodriguez, B. J. (2010). *Rep. Prog. Phys.* **73** 056502.

Kornev, I., Fu, H., Bellaiche, L. (2004). *Phys. Rev. Lett.* **93**, 196104.

Lemée, N., Infante, I. C., Hubault, C., Boulle, A., Blanc, N., Boudet, N., Demange, V., Karkut, M. G. (2015). *ACS Appl. Mater. Interf.* **7**, 19906.

Luk'yanchuk, I. A., Lahoche, L., Sené, A. (2009). *Phys. Rev. Lett.* **102**, 147601.

Lyford, T. S., Collins, S. P., Fewster, P. F., Thomas, P. A. (2015). *Acta Cryst. A* **71**, 255-267.

Nelson, C. T., Winchester, B., Zhang, Y., Kim, S. J., Melville, A., Adamo, C., Folkman, C. M., Baek, S. H., Eom, C. B., Schlom, D. G., Chen, L. Q., Pan, X. (2011). *Nano Lett.* **11**, 828-834.

Paruch, P., Giamarchi, T., Triscone, J. M. (2005). *Phys. Rev. Lett.* **94**, 197601.

Paruch, P., Kolton, A. B., Hong, X., Ahn, C. H., Giamarchi, T. (2012). *Phys. Rev. B* **85**, 214115.

Pietsch, U., Holy, V., Baumbach, T. (2004). *High-Resolution X-Ray Scattering: From Thin Films to Lateral Nanostructures*, Springer.

Schilling, A., Adams, T. B., Bowman, R. M., Gregg, J. M., Catalan, G., Scott, J. F. (2006). *Phys. Rev. B* **74**, 024115.

Schilling, A., Bowman, R. M., Catalan, G., Scott, J. F., Gregg, J. M. (2007). *Nano Lett.* **7**, 3787-3791.

Schilling, A., Byrne, D., Catalan, G., Webber, K. G., Genenko, Y. A., Wu, G. S., Scott, J. F., Gregg, J. M. (2009) *Nano Lett.* **9**, 3359-3364.

Seidel, J., Martin, L. W., He, Q., Zhan, Q., Chu, Y.-H., Rother, A., Hawkridge, M. E., Maksymovych, P., Yu, P., Gajek, M., Balke, N., Kalinin, S. V., Gemming, S., Wang, F., Catalan, G., Scott, J. F., Spaldin, N. A., Orenstein, J., Ramesh, R. (2009). *Nature Mater*. **8**, 229-234.

Sinsheimer, J., Callori, S. J., Bein, B., Benkara, Y., Daley, J., Coraor, J., Su, D., Stephens, P. W., Dawber, M. (2012). *Phys. Rev. Lett.* **109**, 167601.

Stephanovich, V. A., Luk'yanchuk, I. A., Karkut, M. G. (2005). *Phys. Rev. Lett.* **94**, 047601.

Streiffer, S. K., Eastman, J. A., Fong, D. D., Thompson, C., Munkholm, A., Bai, G. R., Stephenson, G. B. (2002). *Phys. Rev. Lett.* **89**, 067601.

Takahashi, R., Dahl, Ø., Eberg, E., Grepstad, J. K., Tybell, T., (2008). *J. Appl. Phys.* **104**, 064109.

Zubko, P., Stucki, N., Lichtensteiger, C., Triscone, J. M. (2010). *Phys. Rev. Lett.* **104**, 187601.

Zubko, P., Jecklin, N., Torres-Pardo, A., Aguado-Puente, P., Gloter, A., Lichtensteiger, C., Junquera, J., Stéphan, O., Triscone, J. M. (2012). *Nano Lett.*, 2012, 12, 2846-2851.

Zubko, P., Jecklin, N., Stucki, N., Lichtensteiger, C., Rispens, G., Triscone, J. M. (2012b). *Ferroelectrics* **433**, 127-137.

Figure captions

Fig. 1. (a) 001 and 002 in-plane q_x-scans. (b) selected 002 in-plane q_x-scans for temperatures raging between 300 and 900, with steps of 50 K (circles: experimental data; line: simulation). The curves are shifted vertically for clarity. (c) schematic representation of the ferroelectric domain structure with alternating up and down polarization with period Λ and wall thickness δ. The black curve is the polarization profile as defined in appendix A.

Fig. 2. Simulated 002 DXS profiles from PT/STO/PZT SLs computed with 250 nm – wide coherent domains, a period Λ = 10 nm and varying domain randomness σ_Λ = 0, 1, 3 nm (rows) and shear strain ε_{zx} = 0, 0.1, 0.3° (columns). In each panel the three curves correspond to increasing values of the tail index η = 0, 0.5, 1 and the red dotted line represent the effect of the wall thickness. The curves are shifted vertically for clarity.

Fig. 3. Simulated 00*l* DXS profiles from PT/STO/PZT SLs computed with a period Λ = 10 nm, domain randomness σ_Λ = 1 nm, shear strain ε_{zx} = 0.1°, tail index η = 0.5 and varying coherent domain size: 50 nm (a), 100 nm (b), 250 nm (c) and 500 nm (d). In each panel the 00*l* (*l*= 1 to 4) curves are plotted from bottom to top and are shifted for clarity.

Fig. 4. (a) evolution with increasing temperature of the out-of-plane component of the polarization normalized to its value at 300 K (filled circles). The red line is a fit with $k(1 - T/T_C)^{1/2}$ (k = 1.3; T_C = 775 K). (b) evolution of the stripe period. (c) evolution of the relative effective wall thickness ($\sigma_w^{(eff)} / w$) and the relative domain randomness ($\sigma_\Lambda / \langle\Lambda\rangle$) as a function of temperature. The blue line is the calculated evolutions assuming σ_Λ = 1.5 nm. The black dotted line is the maximum possible relative wall thickness. The red dotted line is the evolution of the relative roughness $\sigma_R / w = (\sigma_w^{(eff)2} - \sigma_w^2)^{1/2}/w$. The vertical dashed line indicates T_C. The gray areas are the uncertainty regions. (d) schematic representation of a domain wall with finite thickness δ and, (e) of a rough

wall. Both structures give the same average polarization profile along the *x* axis (f).

Fig. 5. (a) evolution of the heterogeneous shear strain (filled circles, left axis) and of the tail index (open circles, right axis). The vertical dashed line indicates T_C and the gray areas are the uncertainty regions. (b) shear strain pdf at RT (blue line) and at T_C (red line) evidencing the narrowing and the suppression of the tails of the distribution with increasing temperature. (c) shear strain cdf at RT and T_C evidencing the confinement of the strain around the average value at RT. The dotted lines correspond to an estimate of maximum shear strain in PZT and PT. (d) schematic representation of 180° stripe domains with flux closure domains. The grey regions indicate the origin of the ferroelastic strain. (e) schematic representation twinned M_C domains with a rotated polarization.

Fig. 1

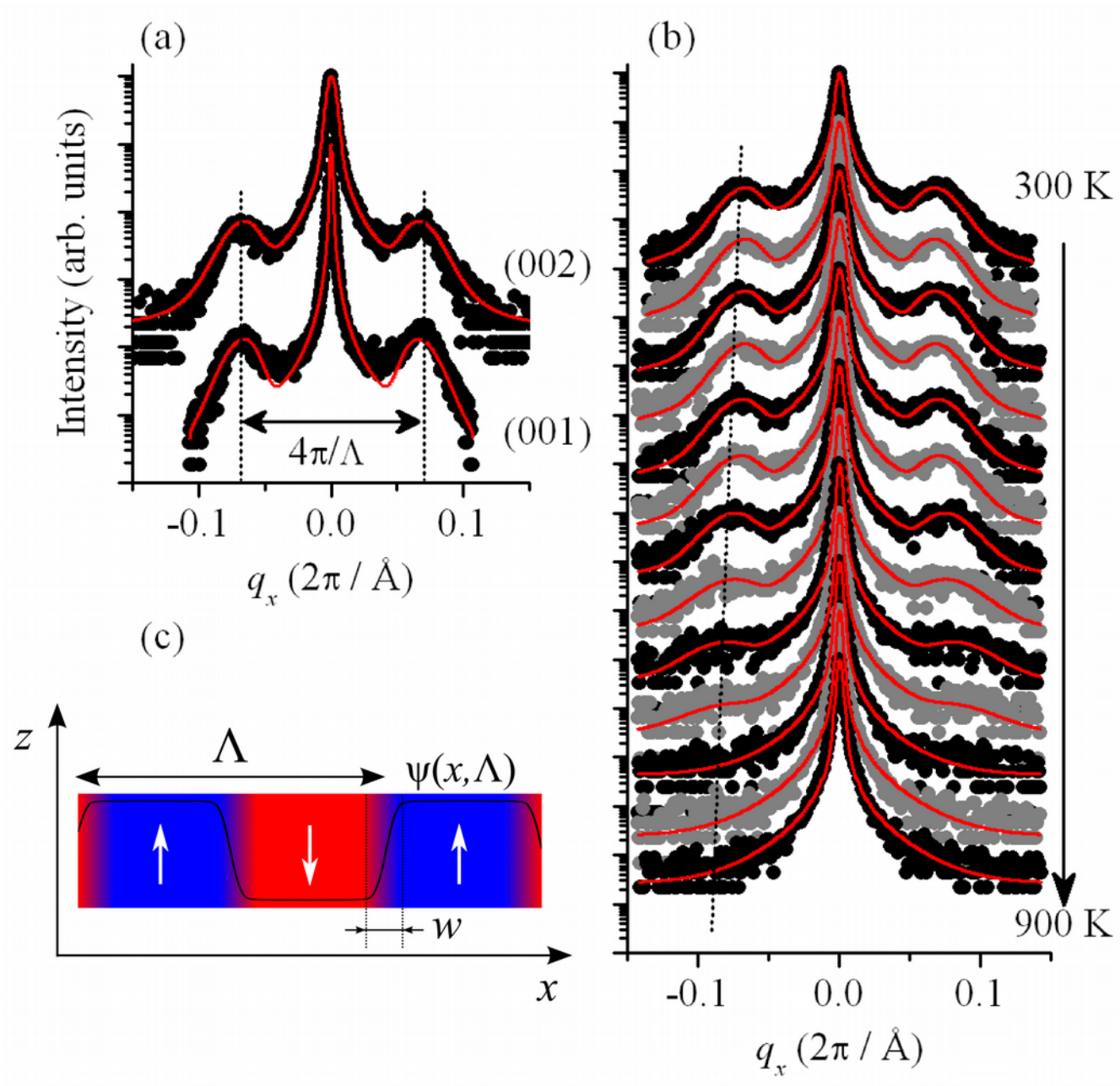
(a)
Intensity (arb. units)
(002)
(001)
4π/Λ
-0.1
0.0
0.1
q_x (2π / Å)
(b)
300 K
900 K
-0.1
0.0
0.1
q_x (2π / Å)
(c)
z
Λ
ψ(x,Λ)
w
x

Fig. 2

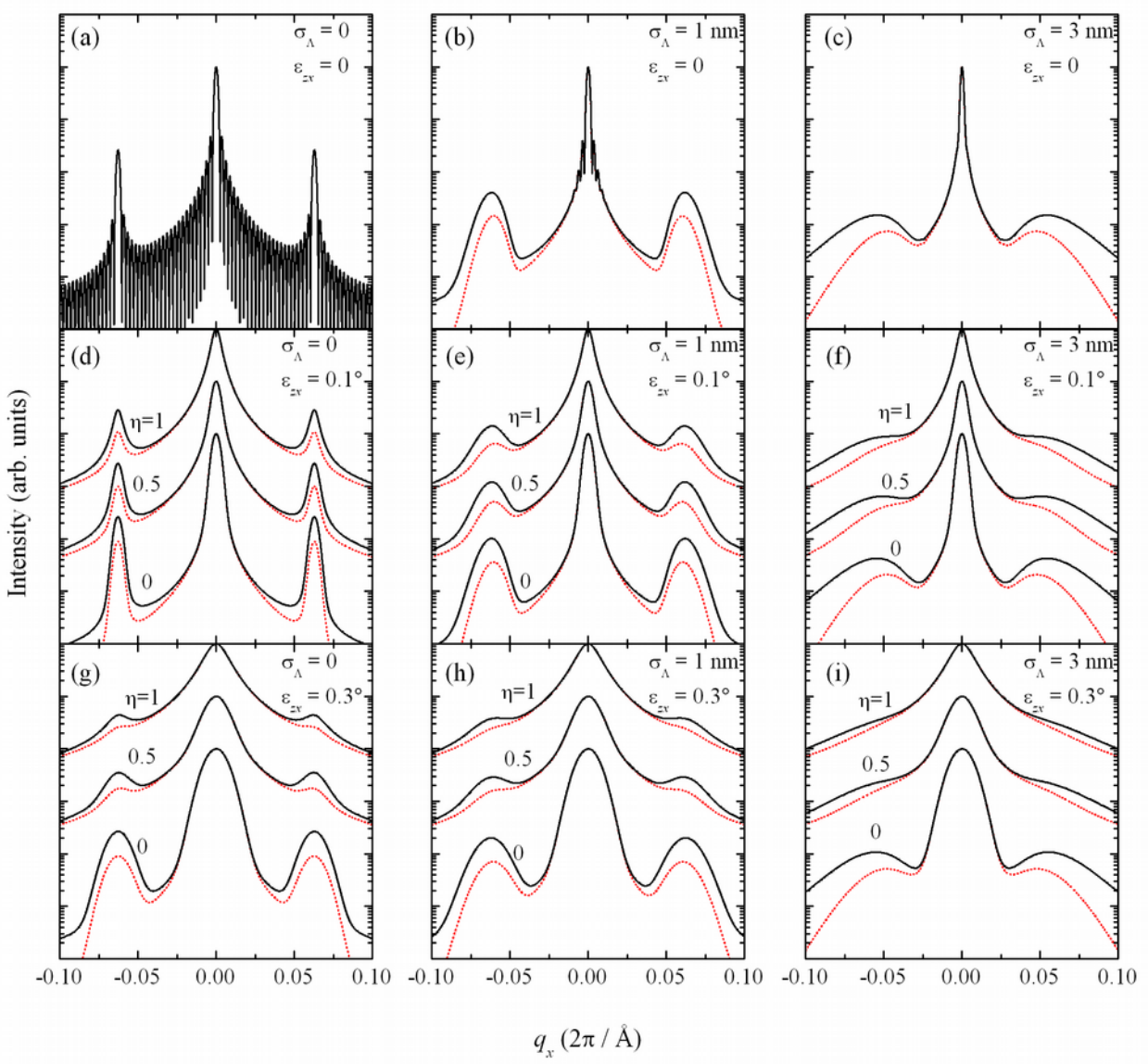
(a)
σΛ = 0
εzx = 0
(b)
σΛ = 1 nm
εzx = 0
(c)
σΛ = 3 nm
εzx = 0
(d)
σΛ = 0
εzx = 0.1°
(e)
σΛ = 1 nm
εzx = 0.1°
(f)
σΛ = 3 nm
εzx = 0.1°
(g)
σΛ = 0
εzx = 0.3°
(h)
σΛ = 1 nm
εzx = 0.3°
(i)
σΛ = 3 nm
εzx = 0.3°
η=1
0.5
0
Intensity (arb. units)
-0.10
-0.05
0.00
0.05
0.10
qx (2π / Å)

Fig. 3

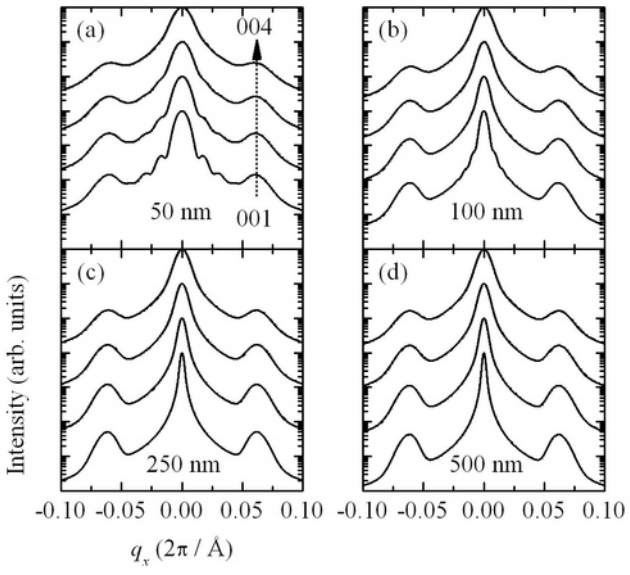
(a)
004
001
50 nm
(b)
100 nm
(c)
250 nm
(d)
500 nm
Intensity (arb. units)
-0.10 -0.05 0.00 0.05 0.10
-0.10 -0.05 0.00 0.05 0.10
q_x (2π / Å)

Fig. 4

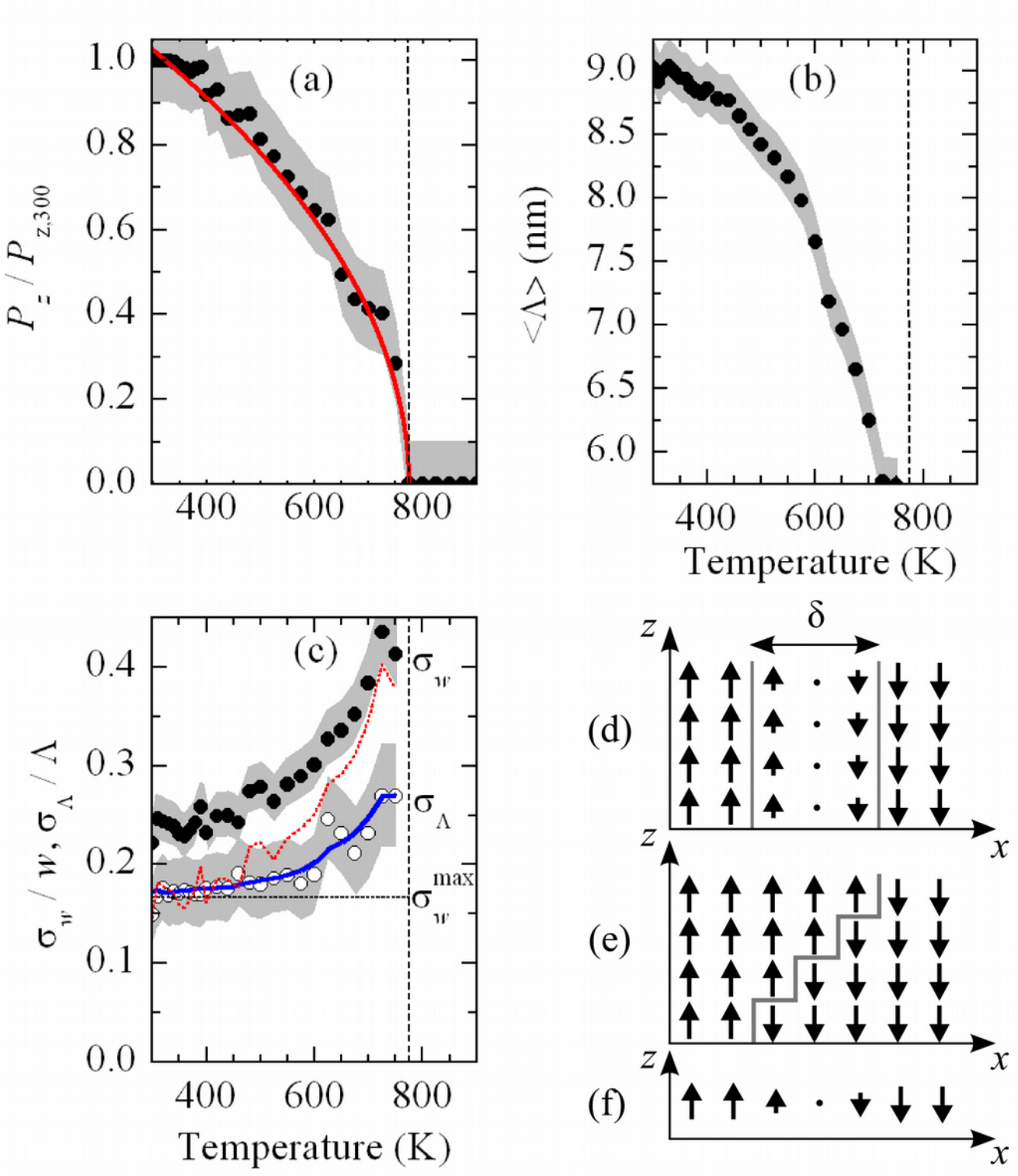
(a)
$P_z / P_{z,300}$
1.0
0.8
0.6
0.4
0.2
0.0
400
600
800
(b)
$\langle\Lambda\rangle$ (nm)
9.0
8.5
8.0
7.5
7.0
6.5
6.0
400
600
800
Temperature (K)
(c)
σ_w
σ_Λ
σ_w^{max}
$\sigma_w / w, \sigma_\Lambda / \Lambda$
0.4
0.3
0.2
0.1
0.0
400
600
800
Temperature (K)
δ
(d)
(e)
(f)
z
x

Fig. 5

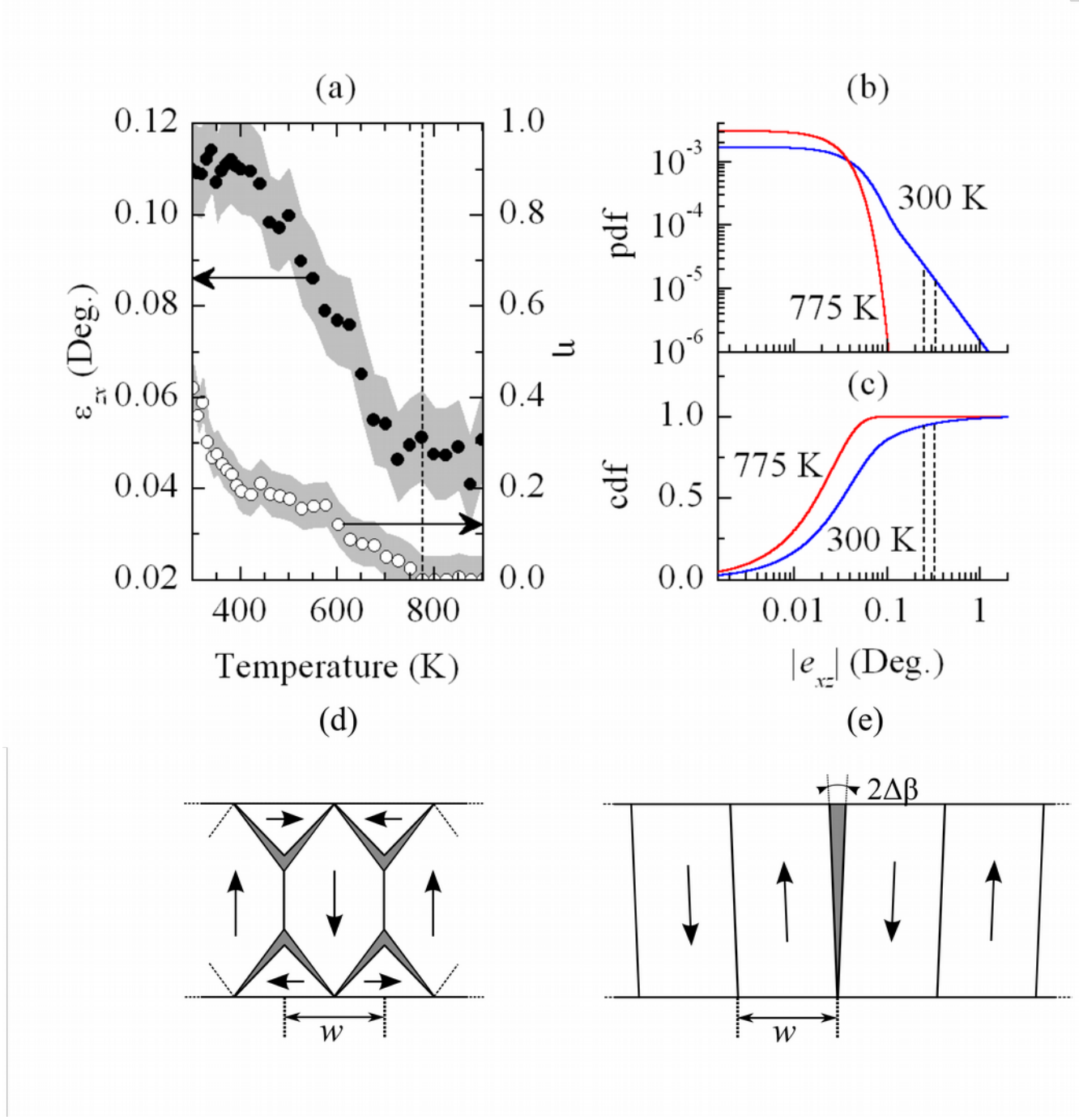
(a)
0.12
0.10
0.08
0.06
0.04
0.02
1.0
0.8
0.6
0.4
0.2
0.0
400
600
800
Temperature (K)
ε_xz (Deg.)
η
(b)
pdf
10^-3
10^-4
10^-5
10^-6
300 K
775 K
(c)
cdf
1.0
0.5
0.0
775 K
300 K
0.01
0.1
1
|e_xz| (Deg.)
(d)
w
(e)
2Δβ
w